ARTICLES
https://doi.org/10.1038/s41563-022-01303-4

nature materials

Check for updates

Tuning colour centres at a twisted hexagonal boron nitride interface

Cong Su[1,2,3,10], Fang Zhang[1,2,4,5,10], Salman Kahn[1,2,10], Brian Shevitski[1,2,3,6], Jingwei Jiang[1,2], Chunhui Dai[1,2,3], Alex Ungar[1,2,3], Ji-Hoon Park[7], Kenji Watanabe[8], Takashi Taniguchi[9], Jing Kong[7], Zikang Tang[5], Wenqing Zhang[4], Feng Wang[1,2,3], Michael Crommie[1,2,3], Steven G. Louie[1,2] ✉, Shaul Aloni[6] ✉ and Alex Zettl[1,2,3] ✉

The colour centre platform holds promise for quantum technologies, and hexagonal boron nitride has attracted attention due to the high brightness and stability, optically addressable spin states and wide wavelength coverage discovered in its emitters. However, its application is hindered by the typically random defect distribution and complex mesoscopic environment. Here, employing cathodoluminescence, we demonstrate on-demand activation and control of colour centre emission at the twisted interface of two hexagonal boron nitride flakes. Further, we show that colour centre emission brightness can be enhanced by two orders of magnitude by tuning the twist angle. Additionally, by applying an external voltage, nearly 100% brightness modulation is achieved. Our ab initio *GW* and *GW* plus Bethe–Salpeter equation calculations suggest that the emission is correlated to nitrogen vacancies and that a twist-induced moiré potential facilitates electron–hole recombination. This mechanism is further exploited to draw nanoscale colour centre patterns using electron beams.

Wide-bandgap materials such as diamond, silicon carbide, gallium nitride and zinc oxide; two-dimensional (2D) semiconductors such as hexagonal boron nitride (hBN) and transition metal dichalcogenides; and one-dimensional nanotubes have all been suggested as candidates for hosting colour centres[1]. These colour centres may provide a basis for quantum computation, quantum information networks and quantum sensors[2]. Colour centres in hBN are particularly noteworthy in that they display emission that is bright[3,4] and stable at high temperature[5], and that has optically addressable spin properties[6,7], with emission spectra spanning across the ultraviolet (UV)[8–11], visible[12–14] and infrared spectral ranges[6]. The van der Waals layered crystal structure of hBN makes it relatively easy to control the thickness through exfoliation[15], which is vital for colour centres as the depth is critical[16]. However, to date, colour centres have still been generally randomly distributed, for example after fabrication by ion bombardment, and their on/off control has been difficult[17,18]. Some success in activating colour centres in hBN has been achieved by applying a static non-uniform strain field[19]. Though optical gating with a laser is an effective method to reversibly activate or deactivate colour centres, as has been demonstrated on nitrogen vacancy centres in diamond and charged defects in hBN[20,21], neither full modulation of the emission amplitude nor brightness control by an external electric field has been achieved. Having such control is essential for utilizing colour centres in sensing and device applications.

Recently, moiré potentials have led to new physical properties in twisted bilayer graphene[22–24] and semiconductor systems[25–28], including new emission peaks[26], electric dipoles[29,30] and nonlinear optical responses[31]. From an engineering perspective, the rotation between hBN flakes is reasonably accessible as a control parameter, as it can be continuously adjusted by a cantilever[32] or a polymer handle[33].

In this work, we show that a UV-emitting colour centre can be collectively activated near a twisted hBN (T-hBN) interface. Using cathodoluminescence (CL) for spectrum acquisition and high-resolution transmission electron microscope (HRTEM) for twist-angle assignment, we find the brightness of this colour centre can be enhanced by two orders of magnitude upon twisting compared with the zero-twist case. We perform calculations employing the ab initio *GW*[34] and *GW* plus Bethe–Salpeter equation (*GW*-BSE)[35] methods to investigate the origin of this colour centre and to provide a physical understanding of the brightness enhancement. Our theoretical analysis leads to an experimental demonstration that an external applied voltage can completely turn off the colour centre and decrease the brightness of the entire detectable UV range (280–409 nm) by 20-fold. We also explain the mechanism of the twist-enhanced colour centre emission and prove it by creating colour centre ensembles with controllable intensity and spatial positioning using electron-beam irradiation. This work thus provides effective methods of activating colour centres around a 2D plane, and, in addition to twist angle, further extends modulation capability to external voltage application and electron irradiation.

Results

To study the effect of twist angle on light emission intensity, we prepare T-hBN samples: one with nearly 0° twist (Fig. 1a) and another

[1]Department of Physics, University of California, Berkeley, CA, USA. [2]Materials Sciences Division, Lawrence Berkeley National Laboratory, Berkeley, CA, USA. [3]Kavli Energy NanoSciences Institute at the University of California, Berkeley, CA, USA. [4]Department of Physics, Southern University of Science and Technology, Shenzhen, China. [5]Institute of Applied Physics and Materials Engineering, University of Macau, Macau, China. [6]The Molecular Foundry, Lawrence Berkeley National Laboratory, Berkeley, CA, USA. [7]Electrical Engineering and Computer Sciences, Massachusetts Institute of Technology, Cambridge, MA, USA. [8]Research Centre for Functional Materials, National Institute for Materials Science, Tsukuba, Japan. [9]International Centre for Materials Nanoarchitectonics, National Institute for Materials Science, Tsukuba, Japan. [10]These authors contributed equally: Cong Su, Fang Zhang, Salman Kahn. ✉e-mail: sglouie@berkeley.edu; saloni@lbl.gov; azettl@berkeley.edu

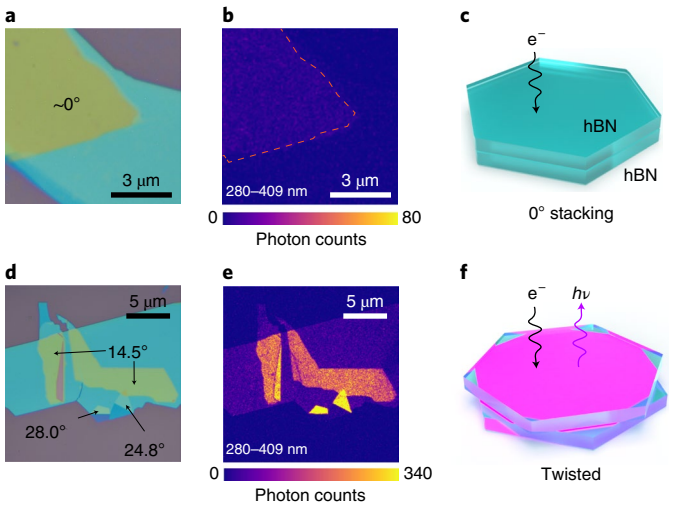

Fig. 1 | Defect emission from T-hBN interface. a–f, The optical images, energy-filtered panchromatic CL intensity map (wavelength window, 280–409 nm) and schematic illustrations of the CL signal in the UV range for stacked hBN flakes with 0° (**a–c**, respectively) and large-angle (>10°; **d–f**, respectively) twist. The twist angles of the T-hBN samples are marked in **d**. Both **b** and **d e** are acquired at the same conditions. e^-, electron; *h*, Planck's constant; ν, the frequency of the photon.

with various twist angles (Fig. 1d). Figure 1b,e shows the intensity of the CL signal integrated between 280 and 409 nm (referred to as a 'UV intensity map' hereinafter) collected by photomultiplier tubes. In Fig. 1b, the stack with nearly 0° twist shows no notable difference in UV light intensity between the stacked area and the pristine top and bottom hBN layers, whereas Fig. 1e displays increased brightness where the hBN top layers are twisted at 14.5°, 24.8° and 28.0° with respect to the bottom layer. The brightness is much higher in the two-layer hBN stacks and increases with the twist angle showing a 50-fold enhancement at 28°. Figure 1c,f schematically illustrates the observation of brightness enhancement due to lattice twist. We have also proved that the emission is localized around the twisted interface (Supplementary Figs. 2 and 3).

Analysis of the spectral signature of the emitted light indicates that it originates from a well-defined colour centre coupled to lattice phonons. Figure 2a compares the CL spectra of the colour centre from single-crystal and T-hBN areas acquired at 35 K. A typical hBN is dark with no emission detectable (yellow curve). The bright UV colour centres, which are very sparsely distributed in bulk hBN, include the emission from the defect itself at 305 nm (4.06 eV), commonly referred to as a zero-phonon line (ZPL), and its phonon sidebands (PSBs) at 321, 336 and 349 nm (3.86, 3.69 and 3.55 eV, respectively) in hBN (red curve). The PSBs are phonon replicas of the ZPL by longitudinal optical phonon at the Γ point[11]. The ZPL and PSB peak assignments are confirmed by temperature-dependent CL, shown in Supplementary Fig. 4, where the intensity of the ZPL increases and that of the PSB decreases when temperature is decreased. Previous studies have demonstrated that this emission originates from a paramagnetic defect in hBN[36], which acts as a single-photon emitter with a second-order correlation coefficient $g^{(2)}(0) = 0.2$ (ref. [10]). The intensity of this emission is substantially enhanced in T-hBN (blue curve).

Figure 2b shows spectra for different twist angles from 0.02° to 25.5°. At the small twist angle (0.02°), no peak is found in the UV range. As the twist angle increases, the intensity of peaks (plotted using conventional non-negative matrix factorization; Methods for details) between 300–400 nm becomes more prominent, with the ZPL staying at 300 nm. Figure 2c shows the brightness of the UV emission (280–409 nm) captured via photomultiplier tubes as a function of twist angle. Samples on both TEM grids (left axis) and SiO_2/Si wafers (right axis) show a similar trend, where the brightness at the interface has a minimum at 0° and is maximized between 20° and 30°. In particular, the emission increases by a factor of 60.5 when the twist angle increases from 0.02° to 27.9°.

Figure 2d,e shows HRTEM images for 0.02° and 12.2° twisted samples, respectively, as representatives of small and large twist angles. For small-angle twisting of 2D materials, crystal distortion and reconstruction is commonly observed[37]. As a result, for the 0.02° T-hBN, we see a honeycomb structure in the low-magnification image and a complete restoration of crystal stacking in the area other than the boundaries of hexagons (the zoomed-in atomic image). In the case of a large-angle twist, like the 12.2° shown here, crystal distortion is not observable, creating homogeneous moiré patterns across the entire T-hBN.

Several conclusions can be made at this point: (1) The 300 nm (or 4.1 eV) ZPL is insensitive to the twist angle and is lower than the band-to-band emission in hBN typically observed at around 210 nm (or 5.9 eV)[38], suggesting it is not a band-edge emission. Our calculation also suggests that the moiré potential cannot decrease the emission from 5.9 eV to 4.1 eV (Supplementary Fig. 9). (2) The emission intensity, on the other hand, strongly depends on the crystal structure (twist angle), suggesting the emission cannot be from the transition between two deep defect levels inside the bandgap of hBN. (3) Compared with other spectrum ranges (inset in Fig. 2b), the intensity enhancement of the defect emission led by the 300 nm ZPL is clearly the most prominent in our sample. (4) Based on the preponderance of emitters around the interface as observed in Fig. 1e, the defect related to the 300 nm ZPL appears to be a commonly pre-existing defect type in hBN.

The origin of the 300 nm (or 4.1 eV) peak has been controversial for over a decade[9,10,39–43]. Experimental results shed some light on it here. First, the emission intensity increases with a decrease of the nitrogen source during synthesis[40]. Second, the 300 nm ZPL appears with the presence of carbon in the precursor during synthesis[36]. These two clues indicate that the nitrogen vacancies (V_N) and substitutional doping of carbon atoms to nitrogen atoms (C_N) or to boron atoms (C_B) are the most probable origins of the deep-UV emission at 4.1 eV (300 nm).

To gain deeper insight into the origin of the defect-driven emission, we adopt the ab initio *GW* and *GW*-BSE approach to calculate the quasiparticle (QP) energies and optical response of the defects, respectively, including electron–electron interactions and excitonic contributions. This approach has been applied with success to a wide variety of materials, including 2D systems with defects[44]. Here, we consider three types of defect structures: V_N, C_N and C_B, based on the above analysis. Figure 2b indicates experimentally that the 300 nm ZPL barely shifts in energy with respect to twist angles, so it is safe to use the defect spectra from a non-twisted hBN calculation to discover the origin of the 4.1 eV emission in T-hBN. To model the isolated defect states, we use the supercell approach that contains approximately 200 atoms (Methods for detailed computational methods).

We present our calculated QP defect energy levels of charge-neutral systems within the bandgap in Fig. 3a. For each type of defect, the defect is spin polarized and there are two QP defect energy levels in the bandgap, corresponding to spin-up (blue) and spin-down (magenta) channels. We use a convention that spin-down QP defect level is occupied while the spin-up level is unoccupied, giving a local magnetic moment of $1\mu_B$ (μ_B, Bohr magneton) for all three defects considered. The calculated optical absorption spectra using the ab initio *GW*-BSE approach (which includes electron–hole interaction or excitonic effects) of bulk hBN containing V_N, C_N or C_B, as well as that of pristine bulk hBN, are shown in Fig. 3b. We validate our method by comparing the experimental band-edge absorption

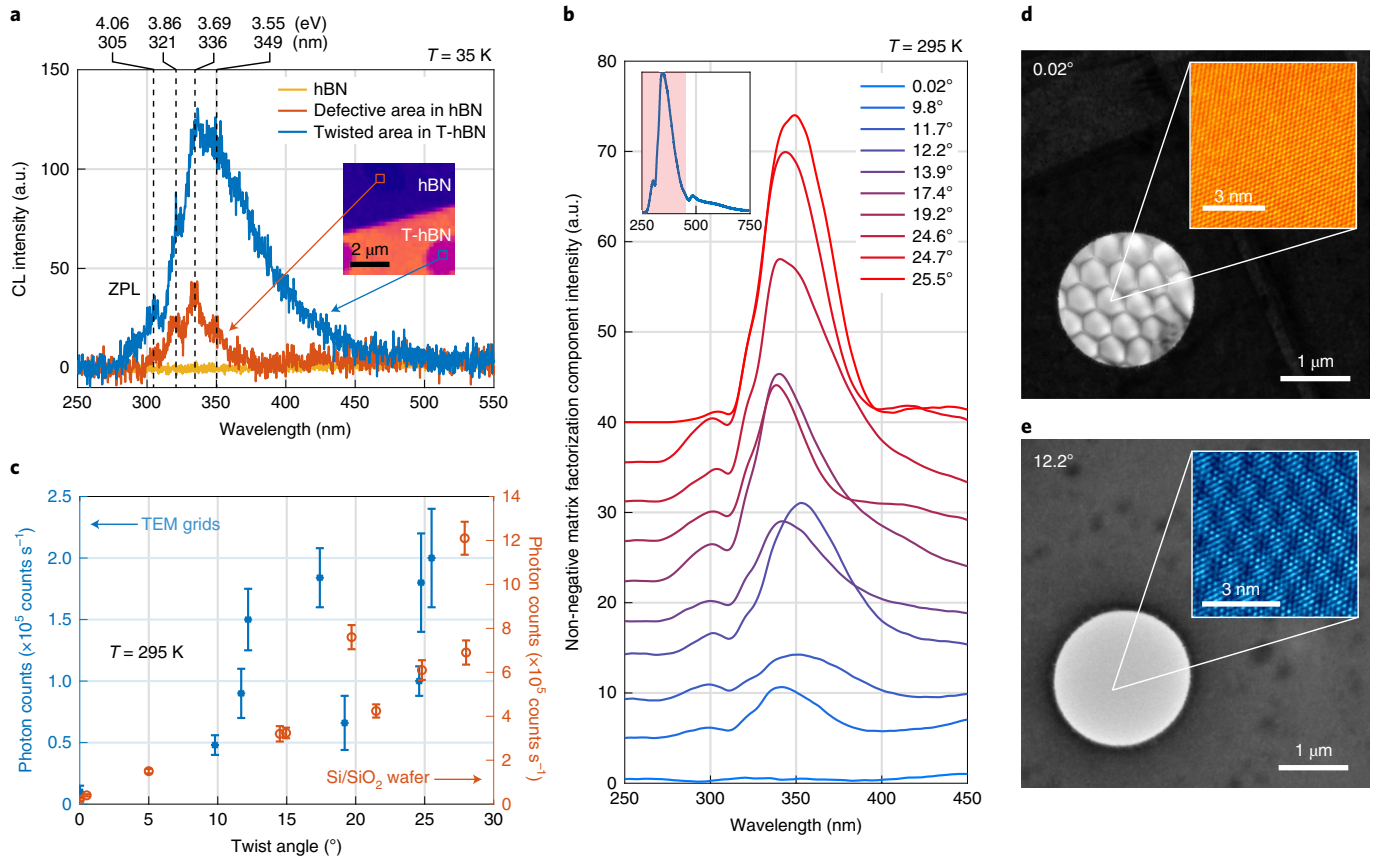

Fig. 2 | Angle-dependent brightness and crystal structures of T-hBN. a, Cryo-CL spectra of the bulk hBN (yellow), defective area in bulk hBN (red) and the twisted area (blue) on the same sample measured at a temperature (*T*) of 35 K. All spectra are from free-standing regions with no substrate underneath. The inset shows a UV intensity mapping showing the locations where the spectra are taken. The round dark holes come from the structure of the TEM grid where hBN or T-hBN is free-standing. **b**, The non-negative matrix factorization decomposition component associated with the CL emission from the T-hBN area at room temperature with various twist angles. The inset shows a typical full spectrum of the T-hBN ranging from 250 to 750 nm. **c**, The increasing trend of the integrated UV intensity in 280–409 nm from photomultiplier tubes when the twist angle approaches 30°. The left and right vertical axes mark the intensity of the free-standing samples on TEM grids (data represented by blue dots) and the samples on the SiO_2/Si substrate (data represented by orange circles), respectively. All data points represent the photon counts per second per pixel, and error bars represent the standard deviations. **d**,**e**, The HRTEM images of the lattice structure of free-standing T-hBN show moiré superlattices with 0.02° twist (**d**) and 12.2° twist (**e**).

peak of bulk hBN from CL (5.81 eV)[38] with our theoretical result (5.79 eV). The match between theory and experiment is extremely good, illustrating the necessity of including many-electron interaction effects in the ab initio calculations. For each defect configuration, the lowest-energy optical bright exciton is denoted by arrows. These excitons should give rise to the peaks that will be the most prominent in emission spectra after excitation of the system[45]. There are two kinds of optically active excitons of distinct character for each type of defect, corresponding to a correlated electron–hole state with (1) a hole in the spin-down QP defect levels and an electron in the hBN spin-down intrinsic conduction states, and (2) a hole in the hBN spin-up intrinsic valence states and an electron in the spin-up QP defect levels. Interaction between these two kinds of excitons is expected to be very weak owing to the spin consideration; thus, the lowest-energy bright exciton of each spin kind would be seen in an emission spectrum. We find that the lowest-energy bright exciton formed between the spin-up defect state in V_N and the hBN intrinsic spin-up valence states has an energy of 4.3 eV with strong oscillator strength (also indicated by the second higher energy blue arrow in Fig. 3b), in good agreement with the 4.1 eV or 300 nm ZPL observed, considering that the *GW*-BSE approximation typically gives an uncertainty in exciton energy of ~0.1 eV. By contrast, the other commonly proposed defects, C_N and C_B, fail to yield any lowest-energy optically active excitons of either kind (1) or kind (2), with energy in the range from 2.5 to 4.9 eV. Therefore, we may rule them out and consider V_N as the origin of the 4.1 eV or 300 nm ZPL.

Two points should also be noted: (1) Even though previous experiments have shown that the 4.1 eV peak correlates with the concentration of C atoms in the precursor[40,46], we believe that a C dopant (especially C_N in a N-deficient environment) is not directly involved in the enhanced emission by twisting. One possible explanation is that C_N encourages more V_N to be created. In the Kröger–Vink notation, $V_N^{\cdots}$ has triple positive charges and C_N' has a single negative charge. As a result, more C_N simply leads to more V_N due to the balancing of charges to make the whole system charge neutral. The rigorously controlled carbon doping experiments[47] and isotopically controlled carbon doping experiments[48] of hBN suggest that the 4.1 eV peak and its PSB are independent of the carbon atoms. (2) In our ab initio *GW* calculations, we assume a fixed lattice for the ground and excited electronic states, which essentially ignores the electron–phonon coupling. The rigid lattice approximation is good for screening defect candidates; however, we expect the predicted emission energy to be even closer to the experimental value if lattice relaxation is considered, as it would essentially lower the energy of the ZPL. The lattice relaxation effect was studied before using constrained density functional theory[49].

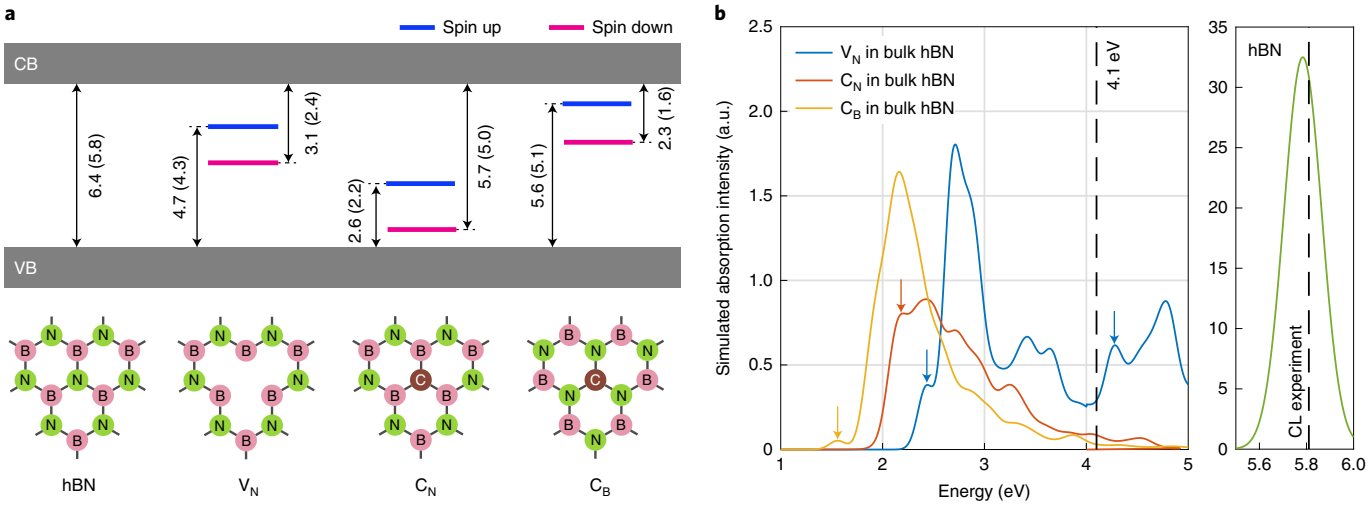

Fig. 3 | Defect type assignment by *GW*-BSE calculation. a, The QP energy levels of V_N, C_N and C_B with respect to the conduction band (CB) and valence band (VB) edges are calculated by the *GW* method. Blue and magenta lines mark spin up and spin down, respectively, using a convention of spin down for the occupied defect state. The numbers next to the double-headed arrows indicate the energetic distance between the energy levels, and the numbers inside the parentheses indicate the energies of the ground-state excitons after subtracting the electron–hole binding energy from the BSE. All the numbers are in units of electronvolts. **b**, The calculated absorption spectra of V_N, C_N and C_B in hBN (left panel) and of pristine bulk hBN (right panel) from ab initio *GW*-BSE. The arrows in the left panel mark the lowest-energy optically bright excitons from each defect type, which would typically dominate the spectra during emission after excitation. The second, higher-energy blue arrow indicates the position of the lowest-energy exciton of another class in V_N that is of a different character from those with smaller energies. The dashed line in the left panel marks the 4.1 eV ZPL of the colour centre, and the one in the right panel marks the edge emission of hBN from CL experiment[38].

Since, according to our calculations, the 4.1 eV ZPL is from exciton states formed with an electron in the V_N defect states and a hole in the hBN intrinsic valence states, the defect emission should have a strong correlation with the excited carrier concentration of the hBN crystal. We confirm this by showing that the brightness of the 4.1 eV emission can be modulated by extracting the excited charge carriers from the system via application of an electric field. Figure 4a shows the vertical layout of the device. The T-hBN sample is encapsulated by two multilayer graphene sheets, which allows for the application of a perpendicular electric field E_t across the sample via application of an external top voltage V_t. A back-gate voltage between the substrate and the bottom electrode can be tuned independently (bottom voltage, V_b). E_t can drive the electron-beam-excited mobile carriers in T-hBN to the two electrodes, giving rise to electron-beam-induced current (EBIC). The EBIC, collected by the electrodes, decreases the carriers available for radiative recombination, thus decreasing defect emission. Indeed, we show that the 300 nm emission is strongly correlated to V_t: When V_t is increased, either positively or negatively, the defect emission is greatly suppressed, as expected (Fig. 4b). The 300 nm emission becomes completely unobservable after V_t exceeds 20 V (Fig. 4c). Only two minor peaks located at 330 nm and 400 nm remain emitting at high V_t, suggesting that these peaks most likely originate from recombination of excitons associated with deep levels rather than involving excited carriers from the band edges. This statement is also supported by time-gated luminescence studies done previously[50]. In Fig. 4d, the anti-correlative relationship of the UV intensity and EBIC as functions of V_t shows that the emission of 300 nm ZPL with its PSB shares a common source with EBIC, which all involve the participation of excited carriers in hBN, making them complementary to each other (Fig. 4e). This complementary relationship between the band-edge carriers and the defect charges is also substantiated by the CL spectrum, where the increase of defect emission is accompanied by a decrease of edge emission (Supplementary Fig. 7). When the amplitude of V_t is above 20 V, a nearly 100% modulation of intensity is achieved for the 300 nm ZPL. In the entire detectable UV range (280–409 nm), about 95% modulation can be reached, with the emission from the two deep-level-state excitons accounting for the remaining 5%. On the other hand, the emission is completely insensitive to the back gate, as expected for a localized emission at the twisted interface (Supplementary Fig. 8). Therefore, by controlling the vertical electric field to be below and above the threshold voltage (V_{th}, around 18 V in our case), we can control the on and off states, respectively, of these emitters, as shown schematically in Fig. 4f.

The enhancement of emission coming from the twist interface originates from what we denote as 'trap-state saturation' because of electronic band structure changes due to moiré potential. In our theoretical analysis, we find that twisting a bilayer hBN system lowers the conduction band minimum (CBM) by 0.2 eV at 21.78°. The valence band maximum (VBM), by contrast, is independent of lattice twisting (Fig. 5a and Supplementary Fig. 10 for more twist angles). The constant energy difference between the localized QP defect state of V_N and VBM explains the unchanged position of the 4.1 eV ZPL at different twist angles in Fig. 2b. In addition, as previous temperature-dependent luminescence experiments have revealed, there are multiple trapping defect states (from different origins) located from 0.1 eV to 0.3 eV below the CBM in bulk hBN, which directly limit the emission of the 4.1 eV ZPL (refs. [36,40]). In larger-twisted-angle T-hBN, a substantial proportion of those trapping states would be energetically above the CBM in the interface region, losing their ability to trap electron carriers located at the CBM locally (Fig. 5b). As a result, the electron-beam-excited electrons in the CBM could be more efficiently scattered into the unoccupied V_N defect level, forming excitons with the holes in the VBM, which leads to stronger emission intensity. The detailed physical origin of these shallow trapping states remains to be explored, but we may tentatively propose one shallow state of V_NC_B as a candidate (Supplementary Fig. 11)[51].

Discussion and outlook

An interesting corollary of the above mechanism is that if we can intentionally saturate the trap states in hBN by a constant external

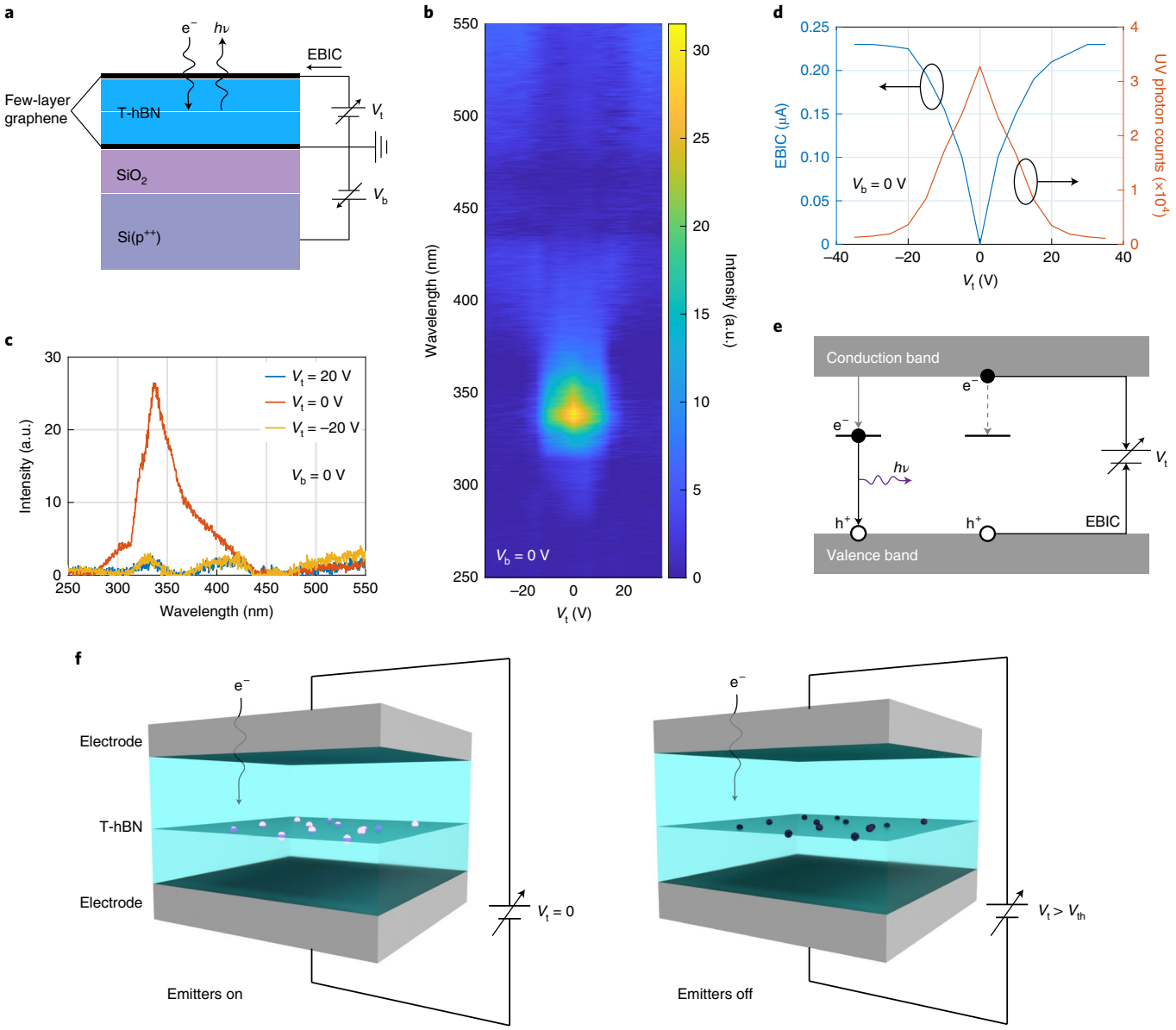

Fig. 4 | Optical modulation of the emitter via external voltage. a, The schematic device structure of T-hBN encapsulated by two few-layer graphene electrodes. The device is biased by two voltage suppliers with the top voltage, V_t, changing the vertical electric field of T-hBN and the bottom voltage, V_b, changing the back gate. Si(p^{++}), heavily p-type-doped silicon. **b**, The colour map of the decomposed CL spectra at T-hBN with V_t ranging from −35 V to 35 V and $V_b = 0$ V. **c**, The spectra of $V_t = 20$, 0 and −20 V from **b**. **d**, The anti-correlative EBIC and UV photon intensity as functions of V_t, with $V_b = 0$ V. **e**, The competing behaviour of EBIC and UV photon emission for mobile carriers. V_t extracts the mobile carriers away from T-hBN, which decreases the formation and hence the recombination rate of excitons (derived from the pairing of electrons in localized defect states and holes (h^+) in valence band states) at the interface. **f**, A schematic of colour centre control through external voltages. When no voltage is applied (left), colour centres at the twisted interface are bright under the excitation source; when voltage is beyond a threshold voltage, V_{th}, the emitters become dark even under excitation (right).

stimulus, say an electron beam, the 4.1 eV emission should also be enhanced as a result. Indeed, we show that this is the case. In Fig. 5c, the colour centre ensembles with 300 nm ZPL are created by parking an electron beam for various dwell times. The spectrum of the electron-irradiated emission is shown in Supplementary Fig. 12, which is nearly identical to the emission of some T-hBN areas. The brightness of UV emission is linearly proportional to the electron dose, though different saturation rates are observed under and above 2.5 s (Supplementary Fig. 13). Controlled creation of the colour centre ensembles can be achieved with a high spatial precision using a guided electron beam, as shown in Fig. 5d, where we draw a smiley face on a single-crystal hBN consisting of 37 ensembles with the same intensity (except for the one on the right, which has a longer exposure time). The mechanism of trap-state saturation using electron beams is shown in Fig. 5e, where we compare the cases of unsaturated trap states before electron-beam exposure (left) and saturated trap states after a substantial electron-beam exposure (right). We find that the colour centre ensembles activated by an electron beam can be annihilated by thermal annealing at 850 °C, where the trapped electrons can be released from the trap states thermodynamically, in agreement with thermoluminescence measurements[36]. This, combined with the fact that a low-voltage electron beam is used, implies that no structural change takes place under the electron beam. As a comparison, the emission at

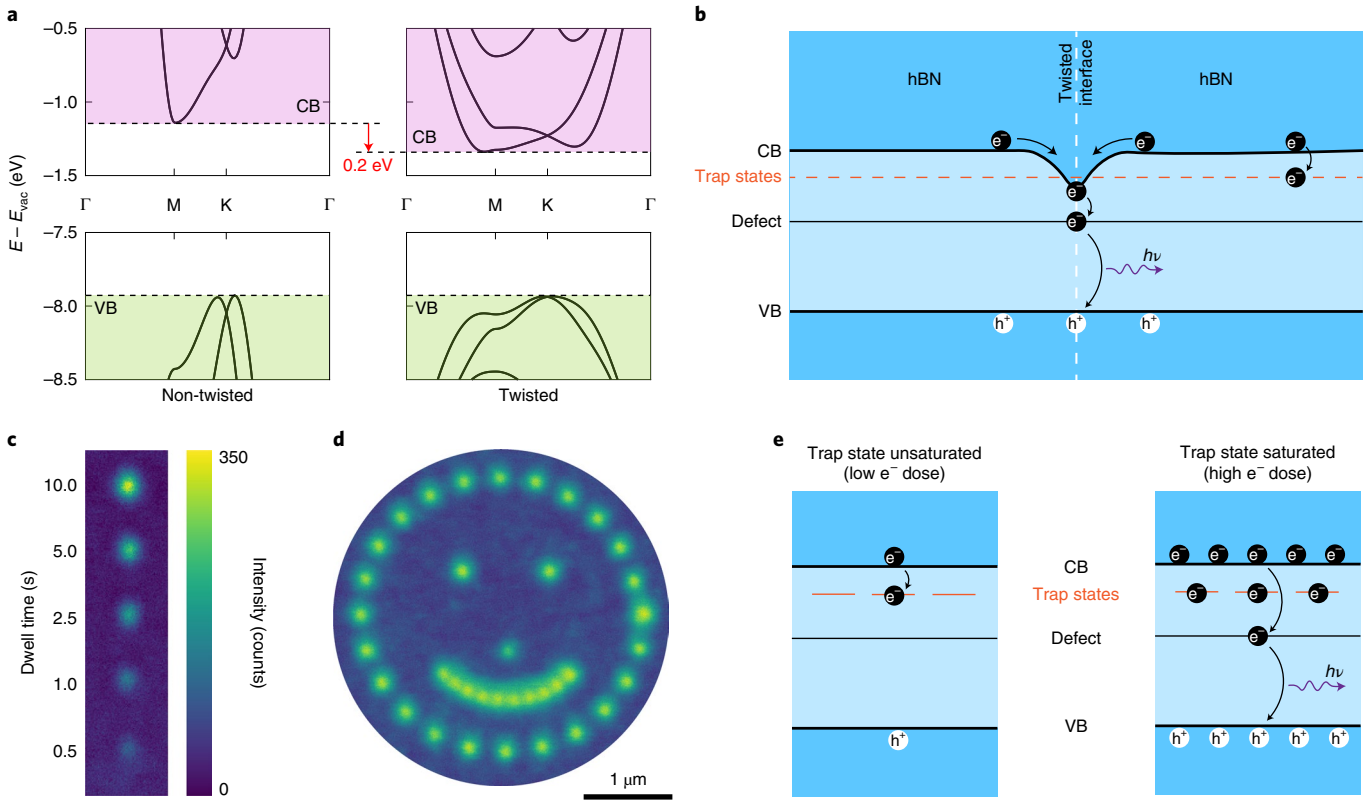

Fig. 5 | Trap-state saturation and electron-beam patterning. a, The band structure changes when bilayer hBN is twisted by 21.78°. The CBM decreases by 0.2 eV, while the VBM is unchanged. *E*, band energy; E_{vac}, ground state energy of an electron in the vacuum. **b**, Upon twisting, the lowering of the CBM creates a quantum well for carrier electrons around the interface, moving the local CBM at the interface close to or even below the shallow trap states. The electrons in the conduction band are thus free from trapping and can go directly to the defect level, forming defect excitons with valence band holes. **c**, An array of colour centre ensembles was seeded with logarithmically spaced dwell times between 0.5 and 10 seconds. The brightness of the colour centre ensemble increases as the dwell time increases, which is a feature of saturating trap states. **d**, The electron beam is placed at a series of locations and dwells for 1 second, resulting in the smiley face pattern. **e**, A schematic of the emission enhancement coming from 'trap-state saturation'. In the left panel, electrons are trapped by trap states without a radiative decay. In the right panel, trap-state saturation leads to radiative decays with UV emission.

the twisted interface is stable under thermal annealing and under electron-beam doping, a direct consequence of the intrinsic saturation (or inactivation) of trap states in T-hBN.

In conclusion, we demonstrate that a colour centre with 300 nm (or 4.1 eV) emission in hBN can be controlled by three different methods: (1) twisting the hBN layers enhances the emission localized around the twisted interface by orders of magnitude, (2) applying an external voltage can modulate the amplitude of emission in the UV range (280–409 nm) by 95% and the 4.1 eV ZPL by nearly 100% and (3) electron-beam irradiation in hBN can continuously enhance the 4.1 eV colour centre ensembles by saturating trap states. The defect responsible for this emission is proposed to be that of V_N, which arises from a 'defect-level/valence-band' exciton according to ab initio *GW*-BSE calculations. We explain the peak intensity enhancement in large-angle T-hBN as being given by an attractive effective potential on the conduction band states created by the interface, where the formation of excitons and their subsequent recombination are facilitated by the lowering of the CBM at the interface to bypass trap states. As quantum information technologies require bright, on-demand and location-determined single-photon emitters, this work paves the way for activating and applying the emitters in a more controllable fashion.

Online content

Any methods, additional references, Nature Research reporting summaries, source data, extended data, supplementary information, acknowledgements, peer review information; details of author contributions and competing interests; and statements of data and code availability are available at https://doi.org/10.1038/s41563-022-01303-4.

Received: 17 October 2021; Accepted: 30 May 2022;
Published online: 14 July 2022

References

1. Aharonovich, I., Englund, D. & Toth, M. Solid-state single-photon emitters. *Nat. Photon.* **10**, 631–641 (2016).
2. de Leon, N. P. et al. Materials challenges and opportunities for quantum computing hardware. *Science* **372**, eabb2823 (2021).
3. Tran, T. T., Bray, K., Ford, M. J., Toth, M. & Aharonovich, I. Quantum emission from hexagonal boron nitride monolayers. *Nat. Nanotechnol.* **11**, 37–41 (2016).
4. Grosso, G. et al. Tunable and high-purity room temperature single-photon emission from atomic defects in hexagonal boron nitride. *Nat. Commun.* **8**, 705 (2017).
5. Kianinia, M. et al. Robust solid-state quantum system operating at 800 K. *ACS Photonics* **4**, 768–773 (2017).
6. Gottscholl, A. et al. Initialization and read-out of intrinsic spin defects in a van der Waals crystal at room temperature. *Nat. Mater.* **19**, 540–545 (2020).
7. Chejanovsky, N. et al. Single-spin resonance in a van der Waals embedded paramagnetic defect. *Nat. Mater.* **20**, 1079–1084 (2021).
8. Shevitski, B. et al. Blue-light-emitting colour centres in high-quality hexagonal boron nitride. *Phys. Rev. B* **100**, 155419 (2019).
9. Museur, L., Feldbach, E. & Kanaev, A. Defect-related photoluminescence of hexagonal boron nitride. *Phys. Rev. B* **78**, 155204 (2008).

10. Bourrellier, R. et al. Bright UV single photon emission at point defects in h-BN. *Nano Lett.* **16**, 4317–4321 (2016).
11. Vuong, T. Q. P. et al. Phonon-photon mapping in a colour centre in hexagonal boron nitride. *Phys. Rev. Lett.* **117**, 097402 (2016).
12. Tran, T. T. et al. Robust multicolour single photon emission from point defects in hexagonal boron nitride. *ACS Nano* **10**, 7331–7338 (2016).
13. Jungwirth, N. R. & Fuchs, G. D. Optical absorption and emission mechanisms of single defects in hexagonal boron nitride. *Phys. Rev. Lett.* **119**, 057401 (2017).
14. Hayee, F. et al. Revealing multiple classes of stable quantum emitters in hexagonal boron nitride with correlated optical and electron microscopy. *Nat. Mater.* **19**, 534–539 (2020).
15. Anzai, Y. et al. Broad range thickness identification of hexagonal boron nitride by colours. *Appl. Phys. Express* **12**, 055007 (2019).
16. Taylor, J. M. et al. High-sensitivity diamond magnetometer with nanoscale resolution. *Nat. Phys.* **4**, 810–816 (2008).
17. Sajid, A., Ford, M. J. & Reimers, J. R. Single-photon emitters in hexagonal boron nitride: a review of progress. *Rep. Prog. Phys.* **83**, 044501 (2020).
18. Son, J. et al. Atomically precise graphene etch stops for three dimensional integrated systems from two dimensional material heterostructures. *Nat. Commun.* **9**, 3988 (2018).
19. Proscia, N. V. et al. Near-deterministic activation of room-temperature quantum emitters in hexagonal boron nitride. *Optica* **5**, 1128–1134 (2018).
20. Geiselmann, M., Marty, R., García De Abajo, F. J. & Quidant, R. Fast optical modulation of the fluorescence from a single nitrogen-vacancy centre. *Nat. Phys.* **9**, 785–789 (2013).
21. Khatri, P., Ramsay, A. J., Malein, R. N. E., Chong, H. M. H. & Luxmoore, I. J. Optical gating of photoluminescence from colour centres in hexagonal boron nitride. *Nano Lett.* **20**, 4256–4263 (2020).
22. Cao, Y. et al. Correlated insulator behaviour at half-filling in magic-angle graphene superlattices. *Nature* **556**, 80–84 (2018).
23. Cao, Y. et al. Unconventional superconductivity in magic-angle graphene superlattices. *Nature* **556**, 43–50 (2018).
24. Sharpe, A. L. et al. Emergent ferromagnetism near three-quarters filling in twisted bilayer graphene. *Science* **365**, 605–608 (2019).
25. Seyler, K. L. et al. Signatures of moiré-trapped valley excitons in $MoSe_2/WSe_2$ heterobilayers. *Nature* **567**, 66–70 (2019).
26. Lee, H. Y. et al. Tunable optical properties of thin films controlled by the interface twist angle. *Nano Lett.* **21**, 2832–2839 (2021).
27. Tran, K. et al. Evidence for moiré excitons in van der Waals heterostructures. *Nature* **567**, 71–75 (2019).
28. Jin, C. et al. Observation of moiré excitons in WSe_2/WS_2 heterostructure superlattices. *Nature* **567**, 76–80 (2019).
29. Woods, C. R. et al. Charge-polarized interfacial superlattices in marginally twisted hexagonal boron nitride. *Nat. Commun.* **12**, 347 (2021).
30. Yasuda, K., Wang, X., Watanabe, K., Taniguchi, T. & Jarillo-Herrero, P. Stacking-engineered ferroelectricity in bilayer boron nitride. *Science* **372**, 1458–1462 (2021).
31. Yao, K. et al. Enhanced tunable second harmonic generation from twistable interfaces and vertical superlattices in boron nitride homostructures. *Sci. Adv.* **7**, abe8691 (2021).
32. Ribeiro-Palau, R. et al. Twistable electronics with dynamically rotatable heterostructures. *Science* **361**, 690–693 (2018).
33. Yang, Y. et al. In situ manipulation of van der Waals heterostructures for twistronics. *Sci. Adv.* **6**, abd3655 (2020).
34. Hybertsen, M. S. & Louie, S. G. Electron correlation in semiconductors and insulators: band gaps and quasiparticle energies. *Phys. Rev. B* **34**, 5390–5413 (1986).
35. Rohlfing, M. & Louie, S. G. Electron-hole excitations and optical spectra from first principles. *Phys. Rev. B* **62**, 4927–4944 (2000).
36. Katzir, A., Suss, J. T., Zunger, A. & Halperin, A. Point defects in hexagonal boron nitride. I. EPR, thermoluminescence, and thermally-stimulated-current measurements. *Phys. Rev. B* **11**, 2370–2377 (1975).
37. Yoo, H. et al. Atomic and electronic reconstruction at the van der Waals interface in twisted bilayer graphene. *Nat. Mater.* **18**, 448–453 (2019).
38. Watanabe, K., Taniguchi, T. & Kanda, H. Direct-bandgap properties and evidence for ultraviolet lasing of hexagonal boron nitride single crystal. *Nat. Mater.* **3**, 404–409 (2004).
39. Wu, J. et al. Raman spectroscopy and time-resolved photoluminescence of BN and $B_xC_yN_z$ nanotubes. *Nano Lett.* **4**, 647–650 (2004).
40. Du, X. Z., Li, J., Lin, J. Y. & Jiang, H. X. The origin of deep-level impurity transitions in hexagonal boron nitride. *Appl. Phys. Lett.* **106**, 021110 (2015).
41. Watanabe, K. & Taniguchi, T. Far-UV photoluminescence microscope for impurity domain in hexagonal-boron-nitride single crystals by high-pressure, high-temperature synthesis. *npj 2D Mater. Appl.* **3**, 40 (2019).
42. Hamdi, H., Thiering, G., Bodrog, Z., Ivády, V. & Gali, A. Stone–Wales defects in hexagonal boron nitride as ultraviolet emitters. *npj Comput. Mater.* **6**, 178 (2020).
43. Mackoit-Sinkevičienė, M., Maciaszek, M., Van de Walle, C. G. & Alkauskas, A. Carbon dimer defect as a source of the 4.1 eV luminescence in hexagonal boron nitride. *Appl. Phys. Lett.* **115**, 212101 (2019).
44. Refaely-Abramson, S., Qiu, D. Y., Louie, S. G. & Neaton, J. B. Defect-induced modification of low-lying excitons and valley selectivity in monolayer transition metal dichalcogenides. *Phys. Rev. Lett.* **121**, 167402 (2018).
45. Pankove, J. I. & Kiewit, D. A. *Optical Processes in Semiconductors* (Dover Publications, 2012); https://doi.org/10.1149/1.2404256
46. Moore, A. W. & Singer, L. S. Electron spin resonance in carbon-doped boron nitride. *J. Phys. Chem. Solids* **33**, 343–356 (1972).
47. Rousseau, A. et al. Determination of the optical bandgap of the Bernal and rhombohedral boron nitride polymorphs. *Phys. Rev. Mater.* **5**, 064602 (2021).
48. Pelini, T. et al. Shallow and deep levels in carbon-doped hexagonal boron nitride crystals. *Phys. Rev. Mater.* **3**, 094001 (2019).
49. Tawfik, S. A. et al. First-principles investigation of quantum emission from hBN defects. *Nanoscale* **9**, 13575–13582 (2017).
50. Museur, L. & Kanaev, A. Photoluminescence properties of pyrolytic boron nitride. *J. Mater. Sci.* **44**, 2560–2565 (2009).
51. Sajid, A., Reimers, J. R. & Ford, M. J. Defect states in hexagonal boron nitride: assignments of observed properties and prediction of properties relevant to quantum computation. *Phys. Rev. B* **97**, 064101 (2018).

Methods

Sample preparation. Heterostructures were fabricated using the conventional 'dry transfer' technique[33,52,53]. T-hBN devices were patterned using standard electron-beam lithography and contacted using electron-beam evaporation of Cr (5 nm) and Au (75 nm). We prepare T-hBN with different twist angles both on rigid SiO_2/Si wafers and suspended over holes in TEM grids for spectrum acquisition. The spectra coming from the suspended (free-standing) T-hBN are free from background noise, whereas the SiO_2/Si wafer contributes a wide spectrum of features in the infrared range; therefore, we present the spectra from the samples on the TEM grids for better accuracy on the line shape, whereas we present data using both substrates for the intensity of UV emission. For the samples on TEM grids, the twist angle of T-hBN is determined by the nanobeam diffraction in HRTEM. More details can be found in Supplementary Fig. 5.

CL. Our customized CL set-up is built on a Zeiss Gemini Supra 55 variable pressure scanning electron microscope. The layout can be found in Supplementary Fig. 1. The experiment is performed by detecting the CL signal using a 5 keV electron beam focused to a ~1 nm spot. Light emitted from the sample is collected by a 3-mm-focal-length parabolic mirror and projected through a quartz window into a light-tight detector array. In the detector array, the light can be coupled into a fibre-coupled Princeton Instruments SP2300i spectrometer through a UV-enhanced parabolic reflector (Thorlabs RC08SMA-F01) and an optical fibre (Thorlabs FG200UEA). Spectra are recorded by a UV-enhanced electron-multiplying CCD (charge-coupled device) camera (Andor 970-UVB). Alternatively, the light can be projected onto a series of photomultiplier tube detectors through multiple long-pass dichroic filters at 409, 482, 543 and 735 nm, generating a series of four bandpass images. A detailed description of the instrument can be found in the Supplementary Information and ref. [8]. The low temperature CL is completed by using a cryo-stage cooled by liquid helium to around 20–30 K. Data have been acquired using home-built software based on ScopeFoundry Python code. Other electron acceleration voltages, including 2, 10, 15 and 30 keV, are also tested with an unobservable difference in CL spectra coming from the T-hBN area.

Spectral decomposition. Spectral maps have been analysed using Python software. Principal component analysis and non-negative matrix factorization have been used to identify the principal spectral signatures from the various regions in the spectral image. We first analysed the weight of each component in principal component analysis and determine the cut-off number of the components to be considered for the spectral decomposition (usually 5–7). We then used a non-negative matrix factorization algorithm to decompose the spectral maps into the spectral components with an output dimension based on the number of components determined by principal component analysis. All components shown in Fig. 2b (except for the 0.02°) come from the component with the highest weight in each spectral map, which matches the T-hBN area.

HRTEM. The atomic-resolution image in the text is obtained from a 200 keV JEOL-2100F field emission transmission electron microscope. The diffraction patterns of different areas are obtained under nanobeam diffraction mode from a 40–60 nm spot size with a less than 200 μrad convergence beam. The twist angles of the sample on the TEM grid are determined by the analysis of the periodicity in moiré patterns for small angles, and by the rotation of (110) diffraction spots in electron diffractograms at angles above a few degrees, where the separation between the diffraction spots is clearly visible. The larger twist angles are determined by the diffraction pattern in TEM, which might correspond to two possible configurations: the two layers can be rotated from either an AA′ or AB stacking order, which is indiscernible by diffraction pattern in multilayer hBN.

Atomic force microscopy. The height of flakes is measured by an Asylum MFP-3D atomic force microscope with an Olympus AC160 cantilever, operated in the a.c. tapping mode.

First-principles *GW* and *GW*-BSE calculations. *Mean-field calculations.* First-principles calculations of the ground state for bulk hBN containing defects and twisted bilayer hBN are performed using density functional theory within the local spin density approximation, as implemented in the Quantum Espresso package[54]. Optimized norm-conserving Vanderbilt pseudopotentials that include semicore states are employed[55]. The Kohn–Sham orbitals are constructed with a plane-wave basis with an energy cut-off of 60 Ry. We use the experimental lattice constants for both the bulk and the bilayer form, with $a = 2.502$ Å and $c = 6.617$ Å, and a vacuum space of 15 Å in a supercell calculation is employed in the bilayer cases. The atom positions are all fully relaxed until the components of the force on each atom are smaller than 0.01 eV Å^{-1}. To mimic defects in hBN, we use a supercell size of $5\times5\times4$ unit cells to prevent interactions between the periodic images of the defect, which contains roughly 200 atoms.

GW calculations. The *GW* (at the G_0W_0 level) calculations[34] are performed using the BerkeleyGW package[56]. For the $5\times5\times4$ supercell bulk hBN containing defects, we use a $2\times2\times2$ k grid, a dielectric cut-off of 15 Ry and 18,000 bands for calculating the dielectric function and the self-energy corrections. For twisted bilayer hBN systems, which are 2D, we adopted a $24\times24\times1$ ($9\times9\times1$) k grid, a dielectric cut-off of 15 Ry and 2,000 (14,000) bands for the 0° (21.78°) twist angle. We treat the dynamical screening effect through the Hybertsen–Louie generalized plasmon-pole model[34].

GW-BSE calculations. To calculate the excitonic states of a $5\times5\times4$ supercell bulk hBN containing defects, the BSE is solved with the electron–hole kernel evaluated from the results of the *GW* calculation. The BSE Hamiltonian[35] is first calculated on a $2\times2\times2$ k grid, and then we interpolate it onto a finer $5\times5\times5$ k grid, diagonalizing the BSE matrix to yield the exciton states.

Electron trajectory simulation and penetration depth calculation. The simulation is done using the CASINO software package, which uses the Monte Carlo method to model the electron trajectory inside the material[57]. The initial electron energies are adopted to be 1, 2, 5, 10 and 30 keV for each round of calculation, and the electron beam is fixed at 1 nm in diameter. The Kanaya–Okayama equation is used for a rough estimation of the electron penetration depth[58].

Data availability

All data are available in the main text or the Supplementary Information.

References

52. Wang, L. et al. One-dimensional electrical contact to a two-dimensional material. *Science* **342**, 614–617 (2013).
53. Zomer, P. J., Guimarães, M. H. D., Brant, J. C., Tombros, N. & Van Wees, B. J. Fast pick up technique for high quality heterostructures of bilayer graphene and hexagonal boron nitride. *Appl. Phys. Lett.* **105**, 013101 (2014).
54. Giannozzi, P. et al. QUANTUM ESPRESSO: a modular and open-source software project for quantum simulations of materials. *J. Phys. Condens. Matter* **21**, 395502 (2009).
55. Tiago, M. L., Ismail-Beigi, S. & Louie, S. G. Effect of semicore orbitals on the electronic band gaps of Si, Ge, and GaAs within the GW approximation. *Phys. Rev. B* **69**, 125212 (2004).
56. Deslippe, J. et al. BerkeleyGW: a massively parallel computer package for the calculation of the quasiparticle and optical properties of materials and nanostructures. *Comput. Phys. Commun.* **183**, 1269–1289 (2012).
57. Hovington, P., Drouin, D. & Gauvin, R. CASINO: a new Monte Carlo code in C language for electron beam interaction—part I: description of the program. *Scanning* **19**, 1–14 (1997).
58. Kanaya, K. & Okayama, S. Penetration and energy-loss theory of electrons in solid targets. *J. Phys. D* **5**, 43–58 (1972).

Acknowledgements

This work was supported primarily by the US Department of Energy, Office of Science, Basic Energy Sciences, Materials Sciences and Engineering Division under contract no. DE-AC02-05-CH11231, within the sp2-Bonded Materials Program (KC2207), which provided for the development of the project concept and theoretical calculations. CL and HRTEM measurements were provided by The Molecular Foundry, supported under the US Department of Energy, Office of Science, Basic Energy Sciences, Materials Sciences and Engineering Division under contract no. DE-AC02-05-CH11231. Additional support was provided by the US Department of Energy, Office of Science, Basic Energy Sciences, Materials Sciences and Engineering Division under contract no. DE-AC02-05-CH11231, within the van der Waals Bonded Materials Program (KCWF16), which provided for sample fabrication, and within the Theory of Materials Program, which provided theoretical methods and analyses. Preparation of the TEM grid suspended samples was provided by the National Science Foundation under grant DMR-1807322. C.S. gratefully acknowledges the financial support of a Kavli Energy NanoScience Institute Heising-Simons Postdoctoral Fellowship. K.W. and T.T. acknowledge support from the Elemental Strategy Initiative conducted by the MEXT, Japan (grant no. JPMXP0112101001) and the Japan Society for the Promotion of Science KAKENHI (grant nos 19H05790 and JP20H00354). W.Z. and F.Z. acknowledge the support from the Guangdong Innovation Research Team Project (no. 2017ZT07C062), Guangdong Provincial Key-Lab programme (no. 2019B030301001), Shenzhen Municipal Key-Lab programme (ZDSYS20190902092905285) and Centre for Computational Science and Engineering at Southern University of Science and Technology. J.-H.P. and J.K. acknowledge the support from the US Army Research Office Multidisciplinary University Research Initiative under grant no. W911NF-18-1-0431 and the US Army Research Office through the Institute for Soldier Nanotechnologies at MIT, under cooperative agreement no. W911NF-18-2-0048.

Author contributions

C.S., A.Z. and S.A. conceived the experiments. A.Z. supervised the whole project. S.G.L. supervised the theoretical studies. C.S. and S.A. designed and performed the regular, in situ and cryo-CL and HRTEM experiments. F.Z. performed the calculations and, with J.J. and S.G.L., performed the theory analyses. S.K. prepared the samples and fabricated the devices. C.D. and A.U. aided in sample preparations. J.-H.P. and J.K. prepared the monolayer hBN samples. K.W. and T.T. provided the bulk hBN samples. C.S. wrote the paper. All the authors were involved in the paper revisions.

Competing interests
The authors declare no competing interests.

Additional information
Supplementary information The online version contains supplementary material available at https://doi.org/10.1038/s41563-022-01303-4.

Correspondence and requests for materials should be addressed to Steven G. Louie, Shaul Aloni or Alex Zettl.

Peer review information *Nature Materials* thanks Sajid Ali and the other, anonymous, reviewer(s) for their contribution to the peer review of this work.